Biomech Model Mechanobiol
DOI 10.1007/s10237-017-0899-1

ORIGINAL PAPER

Affine kinematics in planar fibrous connective tissues: an experimental investigation

C. Jayyosi[1] · J.-S. Affagard[2,3] · G. Ducourthial[4] · C. Bonod-Bidaud[5] · B. Lynch[2] · S. Bancelin[4] · F. Ruggiero[5] · M.-C. Schanne-Klein[4] · J.-M. Allain[2,3] · K. Bruyère-Garnier[1] · M. Coret[6]

Received: 3 August 2016 / Accepted: 15 March 2017
© Springer-Verlag Berlin Heidelberg 2017

Abstract The affine transformation hypothesis is usually adopted in order to link the tissue scale with the fibers scale in structural constitutive models of fibrous tissues. Thanks to the recent advances in imaging techniques, such as multiphoton microscopy, the microstructural behavior and kinematics of fibrous tissues can now be monitored at different stretching within the same sample. Therefore, the validity of the affine hypothesis can be investigated. In this paper, the fiber reorientation predicted by the affine assumption is compared to experimental data obtained during mechanical tests on skin and liver capsule coupled with microstructural imaging using multiphoton microscopy. The values of local strains and the collagen fibers orientation measured at increasing loading levels are used to compute a theoretical estimation of the affine reorientation of collagen fibers. The experimentally measured reorientation of collagen fibers during loading could not be successfully reproduced with this simple affine model. It suggests that other phenomena occur in the stretching process of planar fibrous connective tissues, which should be included in structural constitutive modeling approaches.

Keywords Affine transformation · Constitutive modeling · Fibrous connective tissue · Collagen fibers orientation · Liver capsule · Skin

J-M. Allain, K. Bruyère-Garnier and M. Coret have contributed equally to this work.

Electronic supplementary material The online version of this article (doi:10.1007/s10237-017-0899-1) contains supplementary material, which is available to authorized users.

✉ K. Bruyère-Garnier
karine.bruyere@ifsttar.fr

1 IFSTTAR, UMR_T9406, LBMC, Univ Lyon, Université Claude Bernard Lyon 1, F69622 Lyon, France

2 LMS, Ecole Polytechnique, CNRS, Université Paris-Saclay, Palaiseau, France

3 Inria, Université Paris-Saclay, Palaiseau, France

4 LOB, Ecole Polytechnique, CNRS, INSERM, Université Paris-Saclay, Palaiseau, France

5 Institut de Génomique Fonctionnelle de Lyon, ENS-Lyon, CNRS, Université Lyon 1, Lyon, France

6 LUNAM Université, GEM, UMR CNRS 6183, Ecole Centrale de Nantes, Université de Nantes, Palaiseau, France

1 Introduction

As for most solids, the macroscopic mechanical behavior of soft biological tissues is deeply linked to their underlying microstructural organization (Humphrey 2003; Gasser et al. 2006). For this reason, the development of analytical constitutive equations has been an active research area, in order to obtain structurally based models that relate tissues macroscopic mechanical behavior to their internal structures (Gasser et al. 2006).

Humphrey (2003) gives an extensive review of the contribution of microstructural models to biomechanical and medical applications. Whether they are used for the improvement of surgical techniques (Holzapfel et al. 2002; Chauvet et al. 2010), or the prediction of the aneurysm rupture risk (Gasser 2011), they turned out to be a valuable tool for a wide range of applications.

These models have also a tremendous potential in the field of tissue engineering. Indeed, they can be used to estimate the injury levels of in vivo tissues that the engineered tissue needs to reproduce, or to help ranking the structural properties that are important to mimic (Butler et al. 2001). They may also help to estimate the mechanical signals experienced by the cells seeded in the scaffold (Obbink-Huizer et al. 2014), or

Published online: 29 March 2017

to predict the mechanical consequences of the cell-induced remodeling (Loerakker et al. 2016).

The physiological basis of the microstructural models allows a straightforward incorporation of relevant biological components such as collagen or elastin density, or fibers orientation or waviness. This is a major asset to model processes that directly influence the microstructure like aging or pathologies, by changing adequately the related microstructural parameters (Fung 1990). For instance, a microstructurally based model could take into account the elastin degradation that arises with aging (Robert 2002).

Despite all these advantages and promises, developments of microstructural models present significant challenges. Among them, one of the main concerns is to define how the macroscopic deformation of the tissue will be transmitted to the fiber network at the microscopic scale (Sacks 2003). Indeed, the way the transmission between these two scales is operated will greatly influence the predicted behavior.

In most of the existing analytical models, this is achieved through the affine assumption, which states that the fibers follow exactly the motion of the local volume in which they are embedded. Hence, it presents the major advantage of obtaining the fiber displacement directly from purely kinematic information, without further assumption in the material behavior. This implies that structural phenomena due to the interactions between fibers are not considered as important for the fibers behavior. However, neglecting these phenomena may lead to an over- or underestimate of the fibers strain in the region of interest (ROI) since a part of the fibers displacement may come from interactions and constraints from the surrounding environment.

Experimental investigations of this fundamental assumption are only scarce (Billiar and Sacks 1997; Sacks 2003; Fan and Sacks 2014). This mainly comes from the technical difficulties encountered for the observation of the fibrous microstructure during a mechanical assay, on the same sample and at the same location. Recent advances have been done through the combination of multiphoton microscopy (MPM) with mechanical assays (Screen and Evans 2009; Goulam Houssen et al. 2011; Keyes et al. 2013). MPM is a powerful technique to investigate the three-dimensional architecture of collagen-rich tissues since it offers intrinsic optical sectioning and deep penetration in the tissue. MPM modes of contrast include two-photon excited fluorescence (2PEF) and second harmonic generation (SHG). 2PEF signal comes from elastin fibers and cells or from specifically stained components of the tissue (Deyl et al. 1980; Zoumi et al. 2002). Such specific staining can be used to determine the local strain field (Screen and Evans 2009; Mauri et al. 2013; Jayyosi et al. 2014). SHG specifically reveals the micrometer-scale organization of unstained collagen fibers (Zoumi et al. 2004; Raub et al. 2008; Goulam Houssen et al. 2011). Lately, SHG microscopy has been used in an increasing range of tissues to characterize the microstructural response to mechanical loading, such as skin (Bancelin et al. 2015), liver capsule (Jayyosi et al. 2016), aorta (Keyes et al. 2013), bone (Tang et al. 2015), cornea (Benoit et al. 2016), fetal membrane (Mauri et al. 2015), heart valve (Alavi et al. 2015), nerve (Vijayaraghavan et al. 2014) and tendon (Goulam Houssen et al. 2011).

In this study, the hypothesis of affine transformation is confronted to the experimental data from uniaxial and biaxial mechanical tests on two planar connective tissues. Uniaxial tensile tests have been performed on skin (Bancelin et al. 2015), and elliptic bulge testing has been conducted on liver capsule (Jayyosi et al. 2016). Both experiments have been coupled with multiphoton microscopy imaging, to assess the kinematic of collagen fibers during the test. The local microscopic and macroscopic strains measured are here used to compute the theoretical evolution of the collagen fibers orientation, under the assumption of affine transformation. This theoretical orientation evolution is compared to the observed reorientation during these experimental assays, to assess the validity of the affine assumption.

2 Materials and methods

2.1 Calculation of the theoretical reorientation of collagen fibers

Within the affine hypothesis, the fibers stretch is equal to the tissue stretch in the particular direction of the fibers (Sacks 2003). Consequently, for a fiber family, the strain tensor of the fibers, $\underline{\underline{E}}_{\text{fibers}}$, is given by

$$\underline{\underline{E}}_{\text{fibres}} = \boldsymbol{M}^{\boldsymbol{T}}\,\underline{\underline{E}}\,\boldsymbol{M} \tag{1}$$

where $\underline{\underline{E}}$ is the Green–Lagrange strain tensor applied to the global tissue and $\boldsymbol{M}$ the vector associated with the fiber family direction in the representative elementary volume.

In the following, and when it is not mentioned, the mathematical formulation used is the one reported in Fan and Sacks (Fan and Sacks 2014). We restrict ourselves to planar deformations, since our data were obtained on biological membranes in which the fibers are mostly oriented within the same plane.

To test the affine model, we consider the evolution of collagen fibers orientation in the field of view of the multiphoton microscope during the mechanical test considered (whether uniaxial tensile tests or elliptic bulge tests). A theoretical reorientation under the affine assumption can be calculated based on the initial orientation of the fibers in the region of interest (ROI), and the strain applied to the tissue, as the affine model is purely kinematic.

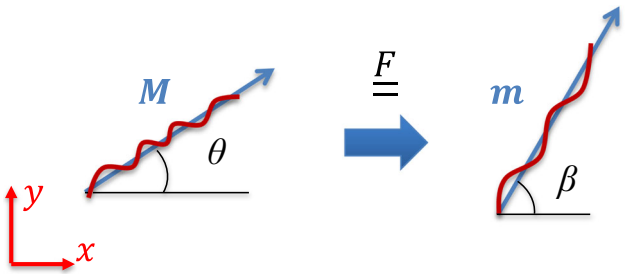


Fig. 1 Reorientation of fiber with main direction **M** in a direction **m** after transformation $\underline{\underline{\mathbf{F}}}$

Let us consider a family of fibers oriented in a direction $\boldsymbol{M}$ defined by an angle θ (see Fig. 1). Setting $\underline{\underline{\boldsymbol{F}}}$ the 2D transformation gradient tensor, the new direction $\boldsymbol{m}$ of this fibers family associated with an angle β after deformation reads

$$\boldsymbol{m} = \underline{\underline{\boldsymbol{F}}}\,\boldsymbol{M} \tag{2}$$

thus

$$\beta = \tan^{-1}\left(\frac{F_{21}\cos\theta + F_{22}\sin\theta}{F_{12}\sin\theta + F_{11}\cos\theta}\right). \tag{3}$$

If we discard the non-diagonal component, we obtain the equation usually used in most reorientation models (Billiar and Sacks 1997; Chandran and Barocas 2005; Rezakhaniha et al. 2012)

$$\tan\beta = \frac{\lambda_y}{\lambda_x}\tan\theta. \tag{4}$$

Let $\Gamma_1(\beta)$ be the fibers orientation distribution in the deformed state and $\Gamma_0(\theta)$, the orientation distribution in the reference state. As adjacent fibers remain adjacent, the number of fibers dN around the angle θ is maintained after reorientation around the angle β

$$\Gamma_1(\beta)\,\mathrm{d}\beta = \Gamma_0(\theta)\,\mathrm{d}\theta = \mathrm{d}N; \tag{5}$$

therefore,

$$\Gamma_1(\beta) = \Gamma_0(\theta)\frac{\mathrm{d}\theta}{\mathrm{d}\beta}. \tag{6}$$

In the general case, the angular derivative is estimated by following the deformation of the surface element associated with a variation of angle dθ around θ into the same element for β, as done by Fan and Sacks (Fan and Sacks 2014). We then obtain, for a 2D transformation

$$\Gamma_1(\beta) = \Gamma_0(\theta)\frac{\boldsymbol{M}^{\boldsymbol{T}} \times \underline{\underline{\boldsymbol{C}}} \times \boldsymbol{M}}{\det \underline{\underline{\boldsymbol{F}}}} \tag{7}$$

with $\underline{\underline{\boldsymbol{C}}}$ the right Cauchy–Green dilation tensor calculated by $\underline{\underline{\boldsymbol{C}}} = \underline{\underline{\boldsymbol{F}}}^{\mathrm{T}}\,\underline{\underline{\boldsymbol{F}}}$.

In the case of a diagonal gradient of the transformation, we get the simple relationship:

$$\Gamma_1(\beta) = \Gamma_0(\theta)\left(\frac{\lambda_y}{\lambda_x}\sin^2\theta + \frac{\lambda_x}{\lambda_y}\cos^2\theta\right). \tag{8}$$

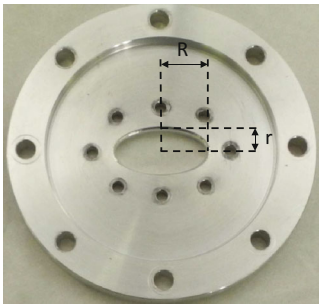
It is thus possible to compute the theoretical reorientation of each direction of the 2D space between $[0, \pi]$ knowing the kinematic of the transformation. The orientation distribution for the deformed configuration is inferred from the orientation distribution of the reference state, associated with the reoriented directions.

2.2 Elliptic bulge test on liver capsule

2.2.1 Experimental setup

The experimental data are based on the experimental work presented in Jayyosi et al. (2016). In this study, bulge tests on human liver capsule were performed under a multiphoton microscope to assess the changes that occurred in the fibrous structure during a biaxial loading. The human liver capsule, or Glisson's capsule, is a thin fibrous connective membrane (40–80 µm thickness) mainly made of type I collagen fibers and elastin fibers (Voss et al. 1980; Gelse et al. 2003). These two fibers networks are deeply intertwined and are considered to define the tissue response to a mechanical loading, which present a nonlinear hyperelastic behavior.

Briefly, a customized air inflation device was developed to perform the bulge test under a two-photon excitation microscope (NIKON, A1R MP PLUS®) at the IVTV platform ("Ingénierie et Viellissement des Tissus Vivants", Engineering and Ageing of Living Tissues, ANR-10-EQPX-06-01). Inflation was conducted with pressure increments of 0.1 bars. After each increment, pauses were taken to allow position stabilization so that there were no movements in the Z direction. SHG and 2PEF signals were then recorded on the entire thickness of the capsule samples. At the same time, the altitude of the apex was collected thanks to the displacement sensor of the microscope objective, to get an estimation of the macroscopic vertical displacement of the sample. In order to test different loading conditions, three configurations of the bulge test were developed: a circular one (referred to as R1), and two elliptic (referred to as R2 for the samples with a ratio 2 between the minor and major axis of the ellipse and R4 for a ratio 4). Therefore, some circular samples ($n = 7$) have been loaded at the apex in an equibiaxial manner, and some elliptic samples (R2 $n = 5$ and R4 $n = 5$) have been subjected to non-equibiaxial loading. The clamp radii for each shape of the experimental setup are given in Fig. 2.



Shape	R (mm)	r (mm)
R1	10	10
R2	12	6
R4	20	5

Fig. 2 Clamp radii for each version of the elliptic bulge test of liver capsule

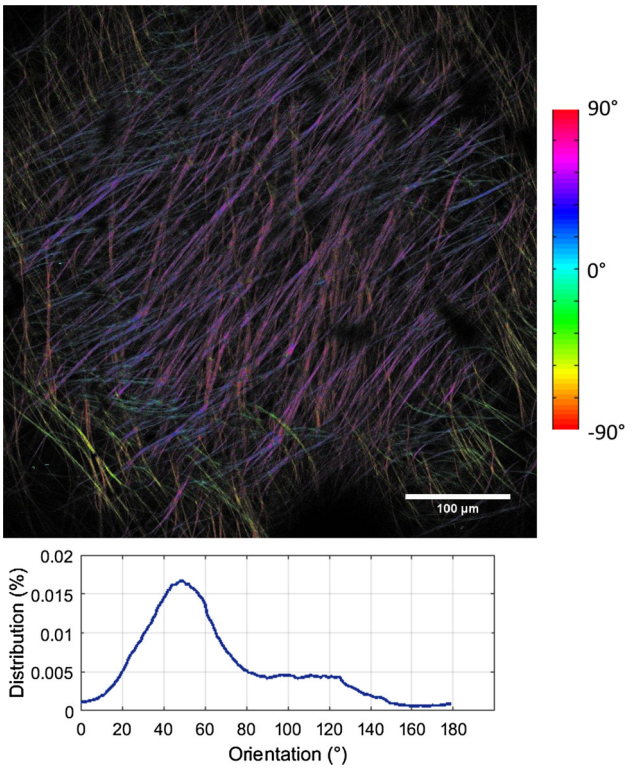


Fig. 3 Calculation of the orientation distribution of collagen fibers thank to the ImageJ plugin OrientationJ developed by Rezakhaniha et al. (2012). *Top* map of collagen fibers with their detected orientation; *Bottom* associated histogram of fibers orientation

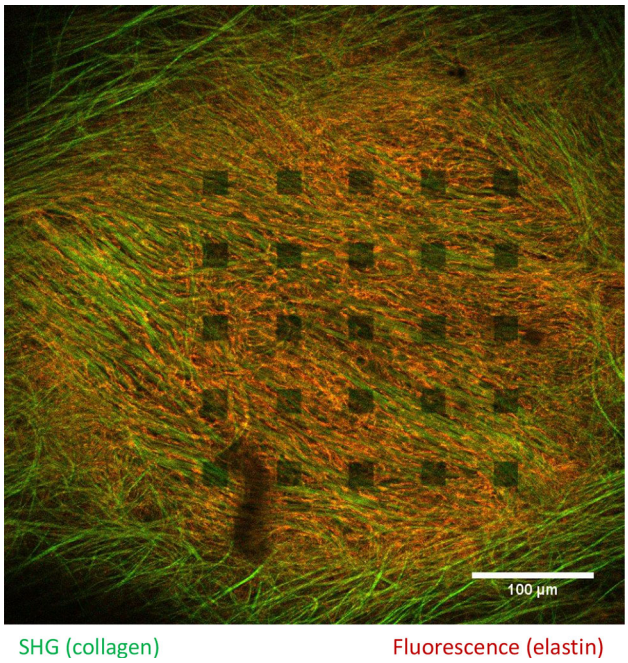


Fig. 4 Typical photobleaching grid made at the apex of a sample of human liver capsule observed with multiphoton microscopy at 0.1 bars. The photobleached squares, characterized by a local loss of fluorescence, are used as nodes of a mesh to compute local strain. Photobleached squares are 20 µm × 20 µm spaced out by 40µm. *Green color* corresponds to the fluorescence channel that shows the elastin fibers, while *magenta color* corresponds to the second harmonic generation (SHG) signal which reveals collagen fibers

2.2.2 *Data analysis and strain calculation*

The collagen fibers orientation distributions were determined on the obtained SHG images (see Fig. 3), at each loading step, using the OrientationJ plugin of ImageJ (Rezakhaniha et al. 2012).

Macroscopic and microscopic measures of strain at the apex were also performed. The microscopic local strain fields at the apex were assessed using the method described previously (Jayyosi et al. 2014). Briefly, a grid of intrinsic markers was created by photobleaching: a 5×5 grid of photobleached squares, as shown in Fig. 4, was made on an area of $260 \times 260\ \mu m^2$ in the field of view (which was $507 \times 507\ \mu m^2$ wide). The grid was positioned at the apex of the capsule after a first pressure increment of 0.1 bars that corresponds to our reference configuration, to ensure an initial uniform curvature of the inflated sample. The photobleaching grid was then imaged at each pressure increments which enabled to investigate the same ROI during the whole test and thus consider the same fibers for the reorientation analysis. The positions of the squared markers were collected at each loading step and used to compute local strain fields using the finite element method.

The macroscopic strain was estimated under the assumption of an ellipsoidal shape of the inflated capsule (Jayyosi 2015). The approximated ellipsoid dimensions were obtained from the apex vertical displacements, measured by the displacement of the microscope objective, and the size of the clamping ellipses. The stretch ratios in X and Y directions, λ_x and λ_y, respectively, were then calculated from the ellipsoid meridian lengths in each direction. These meridian lengths were estimated by the second formula of Ramanujan (Eq. 9), that gives the approximation of an ellipse circumference (Ramanujan 1914):

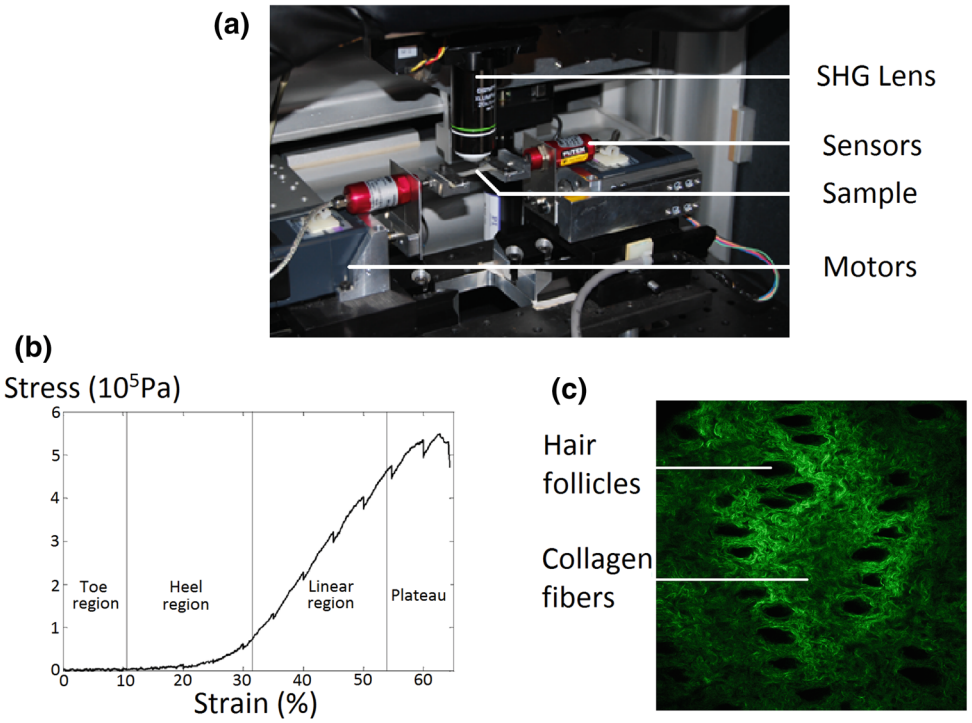


Fig. 5 **a** In situ custom-made tensile test device for skin sample stretching. **b** SHG image of a murine dermis, revealing the hair follicles (*black holes*) and the collagen network (in *green*). **c** Mechanical behavior of the skin under uniaxial tensile testing. The nominal stress versus stretch curve exhibits the four classical regions. The small relaxations are due to the pauses in stretching for image acquisition

$$L \approx \frac{\pi\,(a+b)}{4}\left[1+\frac{3h}{10+\sqrt{4-3h}}\right] \tag{9}$$

with

$$h = \left(\frac{a-b}{a+b}\right)^2 \tag{10}$$

where a and b are the semi-minor and major axes of the ellipse. Thus, a is the vertical displacement of the capsule apex and b the radius of the clamping ellipse in the X or Y direction. The stretch ratios λ_x and λ_y were then obtained by dividing this meridian length by the initial dimension of the clamping ellipse according to the case (R1, R2 or R4). Therefore, λ_x and λ_y correspond to averaged stretch ratios estimated at the apex of the inflated capsule.

Consequently, since we calculated the strain at two different scales, the reorientation calculation was also conducted at two different levels. First the macroscopic strain calculated via the ellipsoidal assumption was used to compute the fibers reorientation on the whole images. The calculation was performed on the distribution of every image of the stack, at each pressure level, with the assumption of a homogenous strain across the thickness. Second, a more local approach was considered by focusing the analysis to the area of the photobleaching grid. Therefore, a measure of the local orientation in each element of the mesh was made, in the mean plane of the grid. The theoretical fibers reorientation was calculated for each element of the mesh, based on the local strain calculated in that particular element.

2.3 Uniaxial tensile test on skin

2.3.1 Experimental setup

The used experimental data originate from (Bancelin et al. 2015), in which uniaxial tensile tests were performed under SHG microscope. Briefly, murine skins were harvested from the back of 4-week-old wild-type mice; epidermis and hair were removed without altering the underlying dermis structure. These samples were cut in bone shape to minimize the clamping artifact and were stretched in situ with a custom-made tensile device (see Fig. 5a). The stress/stretch curves exhibited a classical "J" shape: They had a toe region, a gradual increase (heel region) and a linear section, before rupture (see Fig. 5b). The microstructural organization was assessed by use of a custom-made multiphoton microscope. SHG images ($300 \times 300\ \mu m^2$) showed fibrillar structures corresponding to collagen fibers, interrupted by round structures with no SHG signal corresponding to the hair follicles (see Fig. 5c). As the microstructural image acquisition was impossible during the stretching because of slight movements, loading was performed incrementally (see Fig. 5b), with a pause every 5% of stretching.

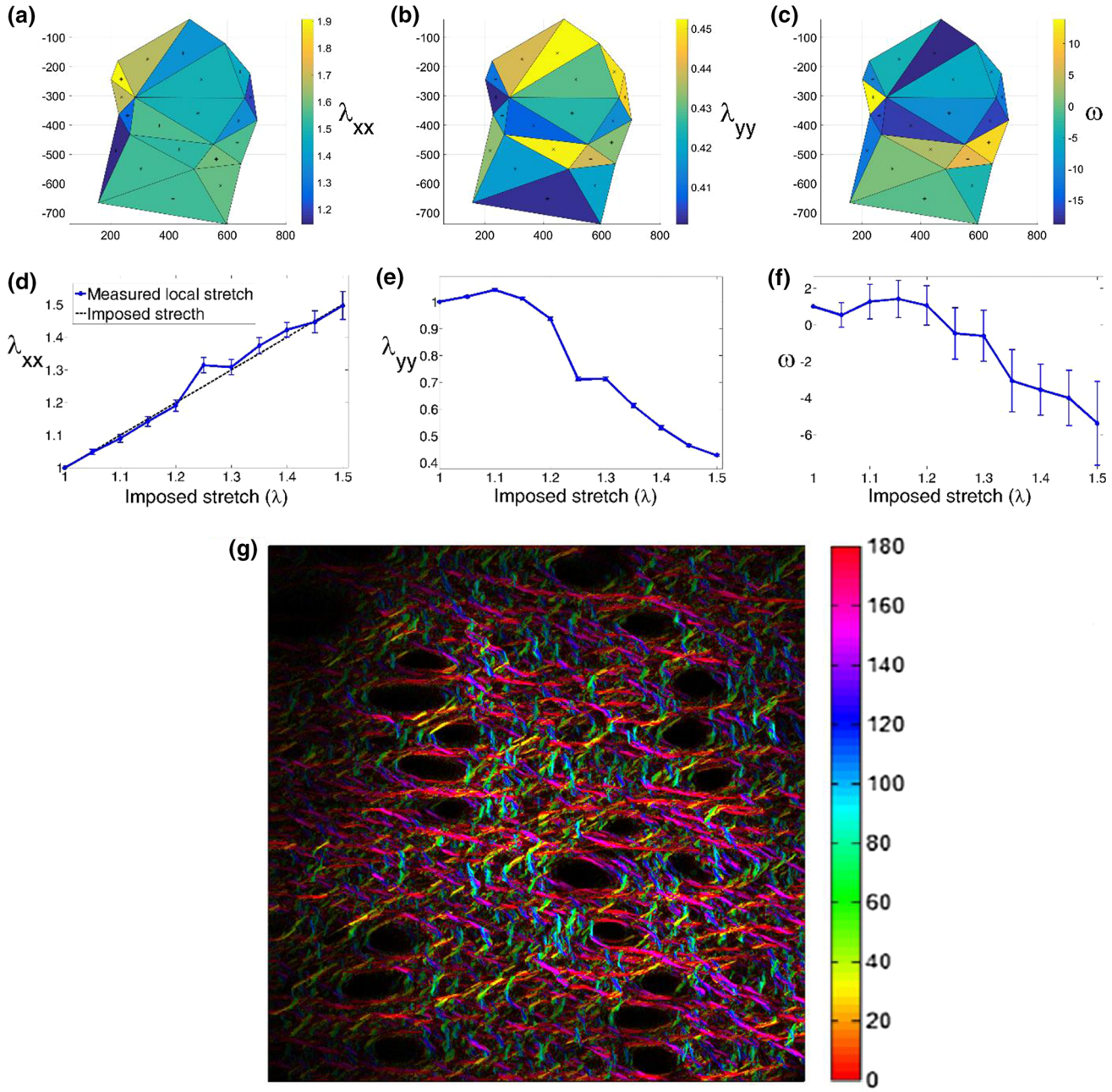


Fig. 6 Analysis of the skin SHG image. **a**–**c** skin local strain on the traction axis (λ_x), transversally (λ_y) and sliding angle (ω), differentiated from the displacements of the hair follicles. **d**–**f** Average values of the surface stretch components (λ_{xx} and λ_{yy}) and the sliding angle (ω) in the SHG image as a function of the global stretch ratio (λ). **g** Collagen fibers orientation, extracted from SHG image

2.3.2 Data analysis and strain calculation

In (Bancelin et al. 2015), the centers of hair follicles were tracked at each stretch level. They defined a Delaunay grid, which was used to compute the local stretch (see Fig. 6a–c).

To reduce the effects of misplaced points, the mesoscopic strain was determined by averaging over the whole region of interest. Figure 6d–f shows the components of the mesoscopic surface stretch tensor (λ_{xx}, λ_{yy}, and the sliding angle ω) as a function of the global stretch ratio (λ). Along the traction direction, the λ_{xx} slope was equal to 1, indicating a homogeneous deformation of the sample. Transversely to the traction direction, the λ_{yy} response was found to be not linear. The initial increase was likely due to structural effects or water absorption; for higher stretch ratios, we observed the expected decrease. At the SHG scale, the sliding angle ω remained small ($<5°$) and thus was neglected to compute the theoretical fibers reorientation.

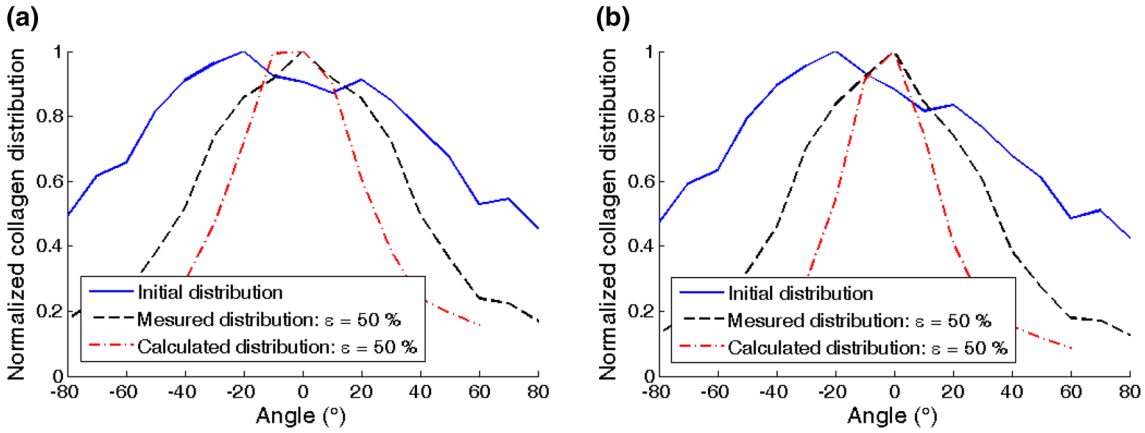


Fig. 7 Distribution of collagen fibers orientation for murine skin, at 50% strain (just before rupture), for samples with a one peak (**a**) and a two-peak (**b**) initial distributions. In each subfigure, the initial distribution of fibers is presented in *blue*, the orientation distribution measured experimentally is indicated in *dashed black*, and the theoretical distribution calculated from the averaged local strain is shown in *dotted dash red*

Independently from the strain analysis, the collagen fibers orientation distribution was extracted from SHG images at each step. A morphological filtering was used to create a map of the fibers orientation (see Fig. 6g) and then a normalized histogram of the fibers orientation distribution was calculated (see Fig. 7) on the field of view.

Using the mesoscopic strain, we computed the theoretical evolution of the normalized collagen fibrils distribution at each level of stretching. To obtain a more quantitative comparison, we used the Orientation Index (OI) scalar (Bancelin et al. 2015). The OI is obtained from the orientation distribution $I(\theta)$ and the angle of the main orientation $\theta_{\max}$:

$$\mathrm{OI} = \left[2 \frac{\int_{-90^\circ}^{90^\circ} I(\theta) \cos^2(\theta - \theta_{\max}) \, \mathrm{d}\theta}{\int_{-90^\circ}^{90^\circ} I(\theta) \, \mathrm{d}\theta} - 1 \right] \times 100 \quad (11)$$

The OI is related to the fraction of fibers aligned with the direction of loading: For a single peak distribution, it is directly related to the width of the pic. It is therefore a useful quantity to analyze the reorientation for uniaxial loading.

We estimated the error on the OI by considering its variation on the five adjacent images of the stack around the position used for its measurement: We found an error of ± 1.

3 Results

Experimental observations gave access independently to the strain and to the fibers orientation distribution at three different scales: (1) the orientation evolution on the whole image (500×500 μm^2) as a function of the strain estimated from macroscopic motions for the liver capsules, (2) the orientation evolution on the whole image (300×300 μm^2) as a function of the local measurement of the strain on the same region for the murine skin and (3) the orientation evolution in 16 subparts of the image as a function of the local strain measured on the same subpart for liver capsule.

In each case, we computed the theoretical distribution of fibers orientation at each strain level using the affine assumption. This distribution is then compared to the measured one.

3.1 Maximal reorientation

3.1.1 Reorientation in the liver capsule for the whole image, based on macroscopic strain

Figure 8 presents the measured initial distribution as well as the theoretical and experimental distributions at the highest pressure level for a human liver capsule. Each subfigure corresponds to a different type of biaxial loading. The examples were chosen so that they display a different initial orientation distribution. Although the analyses were performed on the full stack of images, the figures present only the evolution of a given optical plane of the liver capsule for the sake of clarity.

The main observation is that the affine assumption is not able to predict the reorientation observed experimentally. For the samples that showed an important reorientation during loading ($\sim 30^\circ$, see Fig. 8b), the reorientation calculated from the macroscopic strain is clearly under estimated when compared to the experimental ones. In fact, the strain values measured in these experiments lead to a predicted reorientation of only few degrees. Therefore, the reorientation model derived from the affine assumption can predict the fiber reorientation only for samples that present a limited reorientation ($<10^\circ$, see Fig. 8c).

For circular samples (R1 type), the hypothesis of an equibiaxial loading implied that the stretches were the same in all directions, so the λ_y/λ_x ratio was equal to 1. Therefore, the affine assumption predicted that no reorganization should

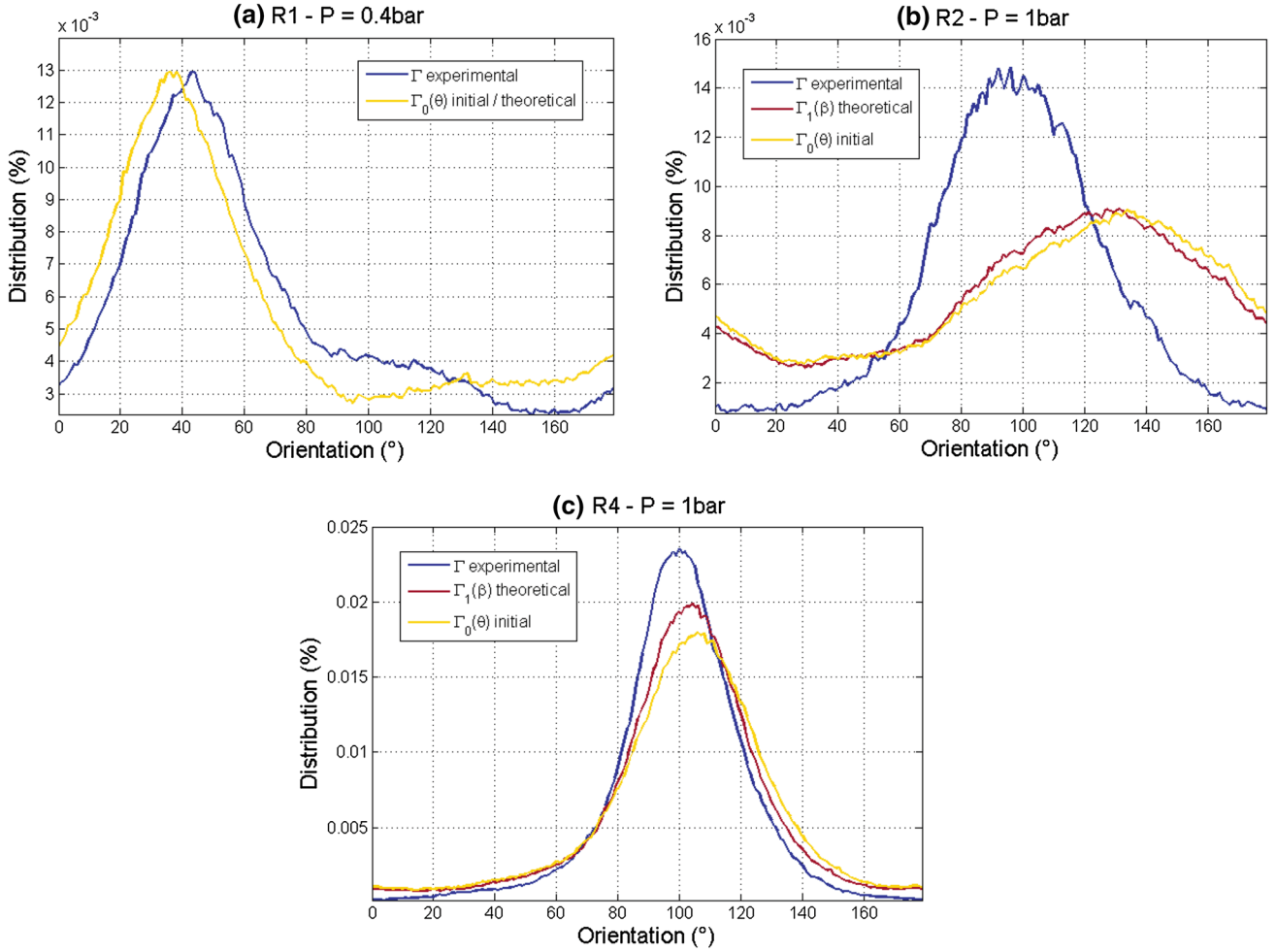


Fig. 8 Distribution of collagen fibers orientation for human liver capsule, at the end of loading (just before rupture), for a circular sample (**a**), an elliptic sample R2 (**b**) and an elliptic sample R4 (**c**). The images were taken in the median plane of the liver capsule. In each subfigure, the initial distribution of fibers is presented in *yellow*, the orientation distribution measured experimentally is indicated in *blue*, and the theoretical distribution calculated from the macroscopic strain values is shown in *red*

occur [$\Gamma_0(\theta) = \Gamma_1(\beta)$ with Eq. 8]. However, a slight reorientation was observed experimentally.

3.1.2 Reorientation in the mice skin for the whole image, based on local strain measured on the same region

Figure 7 presents the measured initial distribution as well as the theoretical and experimental distributions at a high stretch level ($\lambda = 1.5$), close to the rupture stretch for two skin samples. The analysis was performed few micrometers below the surface to have the better signal/noise ratio, but similar results are obtained at the different imaging depths.

In both cases, the fibers are realigned in the direction of traction (0°). The initial distribution had more or less two peaks (around – and + 20°), while the experimental and theoretical final distributions had a single peak centered on the direction of traction. Despite this qualitative agreement, the affine assumption was not able to reproduce quantitatively the observed distribution, which was broader.

3.1.3 Reorientation in the liver capsule for sub-regions of the photobleaching grid, based on local strain measured on the same region

Figure 9 presents the measured initial distributions as well as the theoretical and experimental distributions for each element of the photobleached grid mesh, for the same samples as in Fig. 8. However, the strains used for reorientation calculation were determined locally here unlike Fig. 8. The distributions of the fibers orientation were estimated on the same ROIs as the ones used for the strain determination. As the grid had 5 × 5 points, we had access to 16 sub-regions (which correspond to the 16 elements of the mesh). The posi-

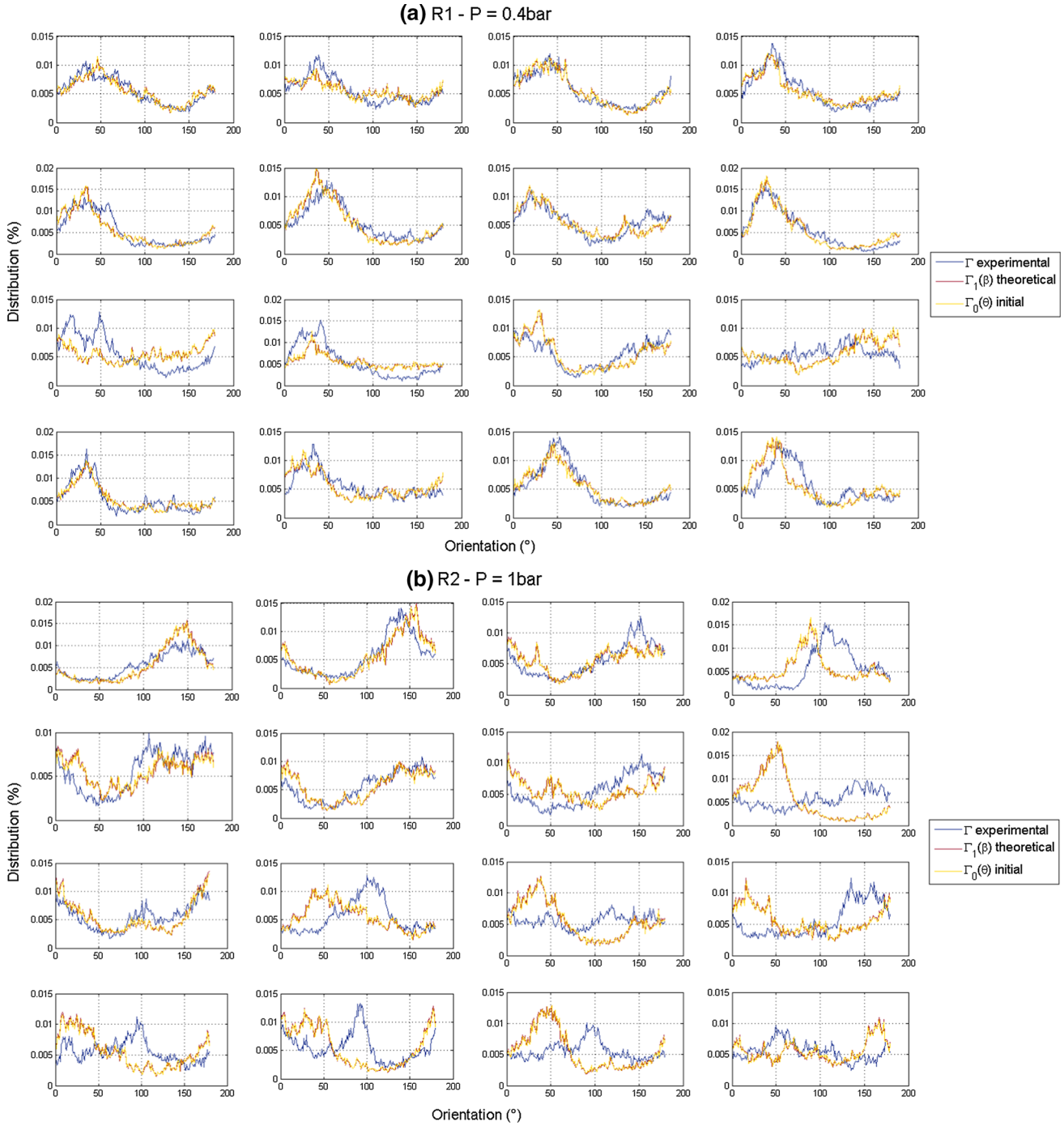


Fig. 9 Experimental (*blue*), theoretical (*red*) and initial (*yellow*) distributions of the collagen fibers in the liver capsule for **a** circular, **b** elliptic R2 and **c** elliptic R4 samples. Each quadrant of the graph corresponds to a different element of the finite element mesh made on the photobleaching grid. Reorientation calculation is based on local strain values. The samples are the same ones as in Fig. 6, at the same pressure level (just before rupture)

tions of the sub-images reported in Fig. 8 correspond to the positions in the photobleached mesh.

Results are quite similar to those observed with the global orientation distribution. For the samples showing no reorientation (see Fig. 9a, c), the small difference between experimental and theoretical orientation distributions that was previously observed in Fig. 8a, c is not present anymore in the different elements of the mesh, or it is smaller than the

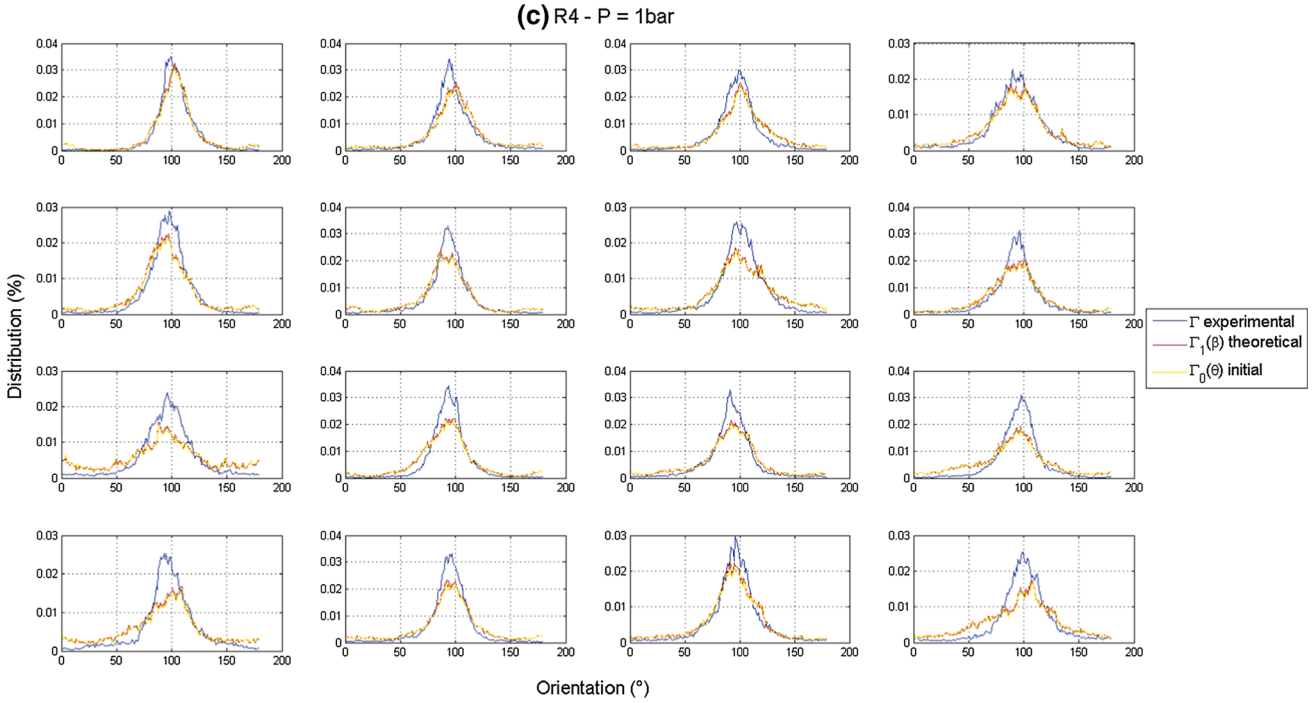


Fig. 9 continued

noise. For the samples where the reorientation was important (see Fig. 9b), results are similar to those from the global orientation analysis, although the reorientation magnitude now depends on the location in the grid.

3.2 Reorientation with strain

The previous examples (see Figs. 7, 8 and 9) were obtained for the highest stretch reached before rupture, where we expected to observe the highest discrepancy between the model and the observations. We now perform similar comparison at intermediate loading steps.

3.2.1 Liver capsule

Regarding the liver capsule, Fig. 10 shows the reorientation observed in the sample R2 (same as in Figs. 8b and 9b), but at a lower pressure level ($P = 0.2$ bars) which corresponds to the beginning of inflation. Figure 10a corresponds to the global reorientation calculated from macroscopic strain (as in Fig. 8b), whereas Fig. 10b presents the local reorientation in the photobleaching grid (as in Fig. 9b).

Not surprisingly, the observed reorientation is lower than the one observed at higher pressure. However, an important gap between theoretical and experimental reorientations is still observed in some areas, for instance in quadrant 8 (2nd row, 4th column) in the Fig. 10b. In quadrant 4 (1st row, 4th column), the beginning of the reorientation process can be observed with the disappearance of the initial dominant orientation into a rather isotropic area. This implies that the discrepancy between the affine assumption and the experimental observations is observed even at small loading values.

3.2.2 Skin samples

Regarding the skin, we have access to a larger number of samples, and to more intermediate stretch levels. Figure 11a, b presents the same results as Fig. 7 but for a lower stretch level ($\lambda = 1.2$) corresponding to the end of the heel region of the stress–stretch curve. A slight difference between theoretical prediction and experimental data is observed in Fig. 11a, the observed orientation remaining very close to the initial one. On the other hand, no difference can be seen between the model and the observation in Fig. 11b, while the experimental orientation no longer corresponds to the initial one.

The same analysis was performed at each step of stretching, for 12 different samples (see Supplementary Figs. 1, 2, 3, 4, 5). Not all samples have reached the highest stretch levels (for example, only four have reached $\lambda = 1.5$): The other ones have broken earlier. We observed that the experimental orientation distributions were close to the initial ones in the heel region of the stress–stretch curve (stress–stretch curves can be seen in Supplementary Fig. 6—the size of the heel region depends on the sample), and became more and more different in the linear region. Not so surprisingly, the predicted distributions were very close to the observed ones

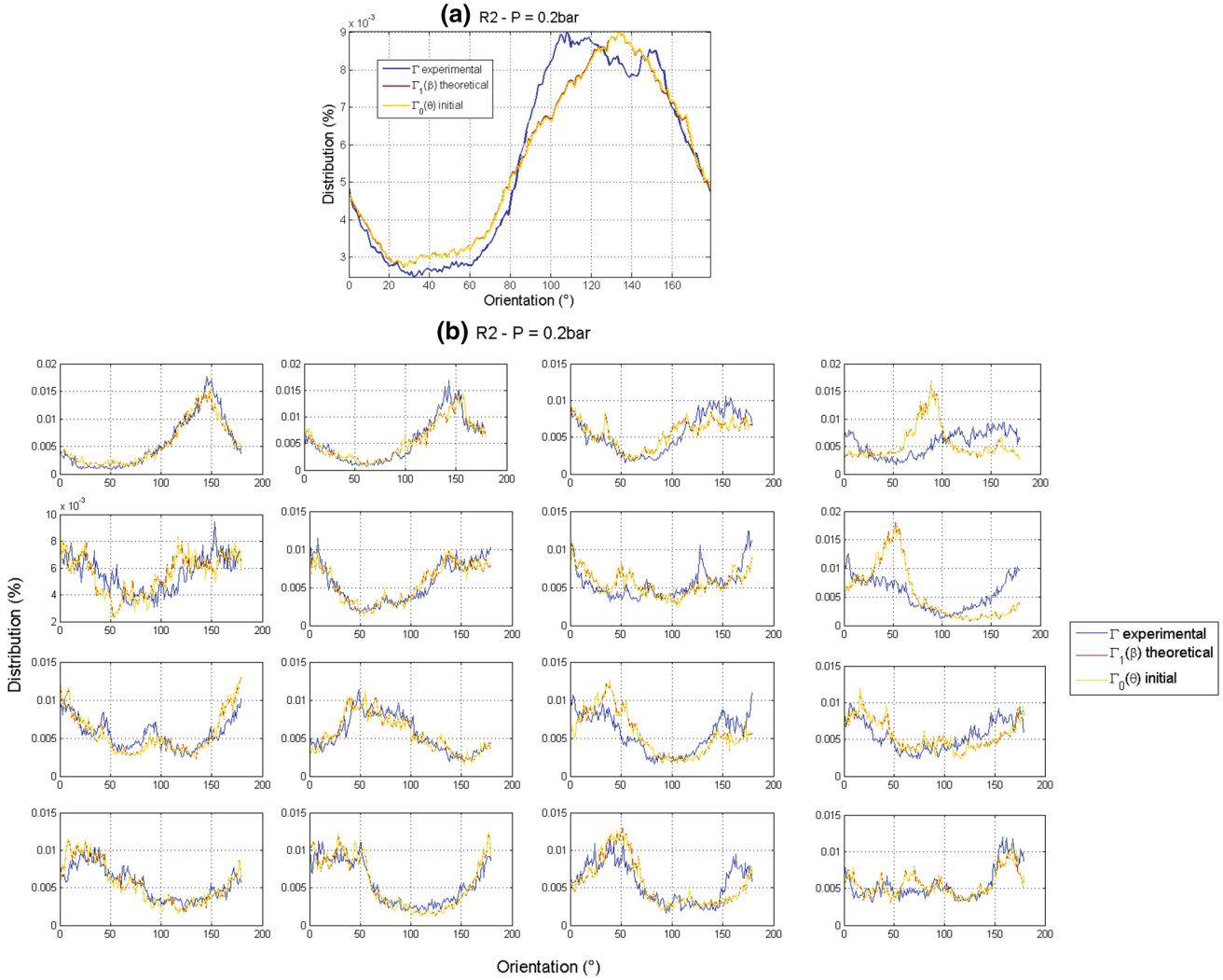


Fig. 10 Experimental (*blue*), theoretical (*red*) and initial (*yellow*) orientation distributions of the collagen fibers in the liver capsule after the first increment of pressure, i.e., $P = 0.2$ *bars*, **a** calculated from the macroscopic strain values and **b** in each element of the finite element mesh calculated from local strain value (each quadrant corresponds to a different element of the mesh). The samples presented here are the same samples as in Figs. 6b and 7b, which presented important reorientation

in the heel region and became more and more different at increasing stretching in the linear region.

Figure 12a, b shows the evolution of the experimental and predicted Orientation Index, and the difference between the two. We observed a double part behavior: at low stretches, we did not observe a significant difference between the experimental and predicted OIs; at higher stretches, the difference progressively increased. This behavior was found in almost all our 12 analyzed samples (see Supplementary Fig. 7).

4 Discussion

We have tested the validity of the affine assumption with respect to experimental observations in two planar fibrous tissues. The affine assumption is used in most multiscale models of connective tissues to relate the motions and stretches of the collagen fibers to the ones of the material volume embedding these fibers. Indeed, it is the simplest and most natural assumption since it supposes that the fibers follow exactly the kinematic of the representative elementary volume. Within this assumption, the knowledge of the transformation kinematics is sufficient to completely determine the kinematics of the collagen fibers.

We used multiphoton microscopy combined to mechanical assays to image the collagen fibers organization at different stretch levels. This was performed on two different tissues: the Glisson's capsule of human livers and the dermis of murine skins, which were subjected to, respectively, biaxial and uniaxial tensile tests. The multiphoton

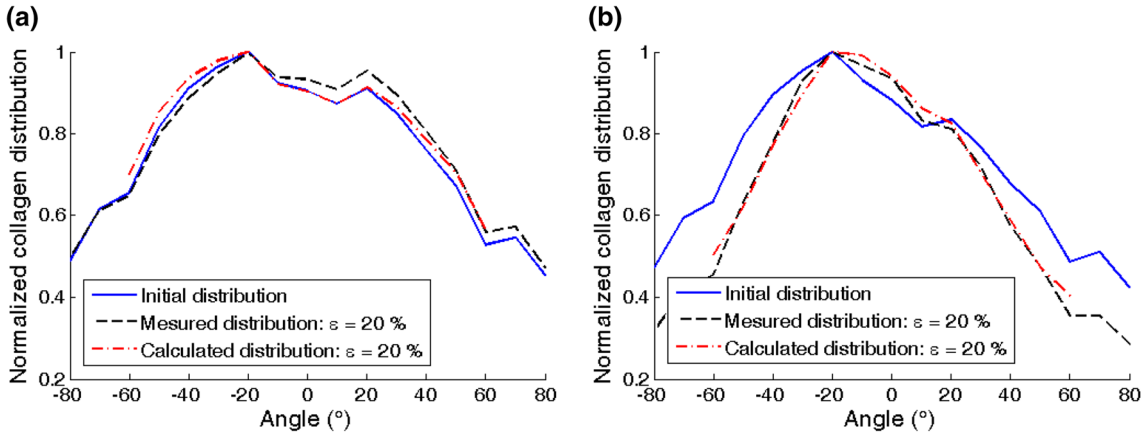


Fig. 11 Reorientation of the collagen fibers at low strain for murine skin samples. Initial orientation distribution of fibers (*blue*), experimentally measured orientation distribution (*dashed black*) and theoretical distribution calculated from the averaged local strain (*dotted dash red*) for the same samples as the ones in Fig. 7, for a strain of 20%

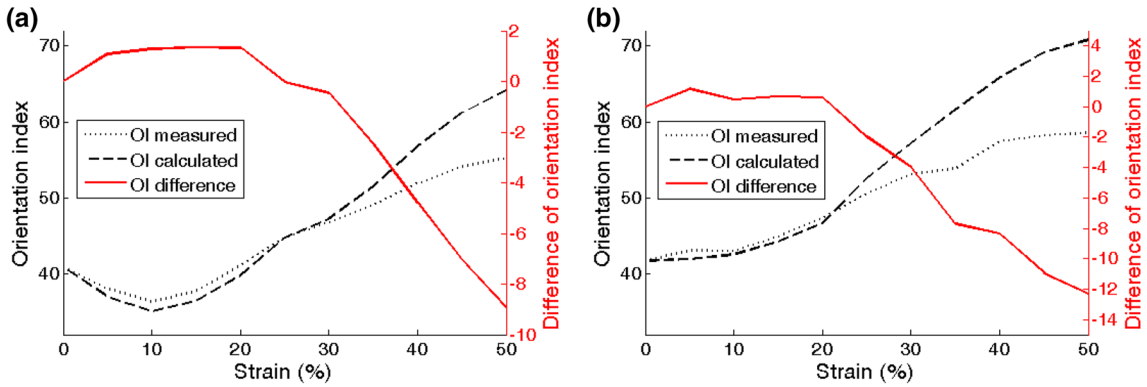


Fig. 12 Evolution of the OIs measured (*dotted black*) and calculated (*dashed black*), and their difference (measured minus calculated) (*red*), as a function of the applied strain, for the same samples as the ones in Fig. 7

microscopy and more specifically the SHG contrast provided volume images of the collagen fibers with a micrometer resolution. We used these images to extract the fibers orientation in a ROI (the whole image or subparts). Therefore, we had access to a series of collagen fibers orientation distributions at increasing stretch levels.

The approaches we used were efficient to determine the planar orientation of the fibers. Effects of curvature (for liver capsule) or out-of-plane inclination of the fibers were not taken into account. Indeed, at the scale of the whole image, we did not observe significant bending of the liver samples, even at high load. The out-of-plane inclination of the fibers could exist, but is expected to be small in planar tissues. Moreover, we had no reason to assume that the reorientation would be more accurately predicted for out-of-plane motions than for in-plane motions, while the full 3D analysis would require a higher resolution in the z-direction than the one used here. The same ROI was observed during the whole experiment. Still, as the tissue was stretched, it became thinner which implied that more and more fibers were observed in the same plane. As we did not observe any difference in the fibers orientation distribution along the thickness of the sample, and as we used normalized distribution, this effect was not likely to create a significant bias in our data.

Independently, we determined the stretch of the ROI, based on other information obtained from the microscope: displacement of the centers of the hair follicles for the skin samples, and displacement of the apex or of a photobleached grid in the fluorescence channel for the liver samples. The knowledge of the strain and of the collagen fibers orientation histogram on the reference image was sufficient, in the affine assumption, to determine the orientations of the fibers at each stretch level.

In the affine assumption, there is no assumption on the tissue behavior (elastic, fluid or viscoelastic), just that the fibers follow the strain of the volume in which they are embedded. Thus, a possible test could have been to observe a modification of the fiber orientation during the tissue relaxation, at

a fixed volume (for liver) or strain (for skin): the observation of a reorganization of the network at fixed strain implies that the assumption is not valid. We could not perform such observation, as the images were taken after a brief relaxation period in order to stabilize the specimen. However, we still observed the microstructure during that relaxation period, in a degraded imaging mode. This was necessary to track the same location on the sample and image the same ROI. We observed qualitatively mostly rigid-body displacements, no in-plane strain and no fiber motions. Still, some reorganization is expected in order to account for the viscoelastic mechanical behavior, and several explanations can be given as why this reorganization is not observed. First the stress relaxation may be explained by the fluid exudation (Lanir et al. 1988; Hannafin and Arnoczky 1994); second, the stress may relax due to cross-bridges detachment and reattachment (Puxkandl et al. 2002), relaxing stresses inside or between fibers but without deformation of the network at the scale we are probing; third, the reorganization during the relaxation could also exist but be limited and not visible in such qualitative way. It is also possible that the reorganization occurs outside of our ROI, but this sounds unlikely, at least for skin where the strain was found to be homogeneous.

We had three approaches for the strain calculation, based on the specificity of each tissue. Clearly, the macroscopic measurement used on liver capsule was the less accurate, since it relied on strong assumptions, investigated in Jayyosi's thesis (Jayyosi 2015). First, the motion of the apex of the sample was determined by the vertical displacement of the focal plane. Comparison with stereocorrelation images showed an average error of -0.35 mm, leading to an underestimation of the strain down to -5%. This can lead to an underestimated reorientation. Second, the boundary conditions could create heterogeneous strains and induce an extrinsic non-affine kinematic that would not come from structural phenomena. In fact, the slight reorientation of circular samples observed in Fig. 8a may come from heterogeneities in the radial strains induced by a non-uniform clamping, which would modify the equibiaxial loading into a non-equibiaxial tensile test. The difficult control of the boundary conditions was indeed highlighted during stereoscopic digital image correlation tests (Jayyosi 2015).

Local measurements seemed much more promising, although harder to perform. Two different methods were used, selected on the specificities of the tissues. For liver samples, we photobleached a grid since this tissue exhibited an important fluorescence signal coming from the non-collagen matrix. Then, the displacement of the grid was tracked using classic DIC approaches and used to determine the strain in each of the 16 subparts of the grid. Skin samples did not show a fluorescence background, but exhibited well-defined endogenous structures: the hair follicles. So, we tracked the center of each follicle, creating a grid on which we computed the strain. As the follicles were not uniformly distributed, and as their position tracking was not perfect, we averaged the computed strains on the whole image, which was less sensitive to measurement errors and provided parameters at the same scale for all samples.

We had thus access separately to an observed and a predicted histogram of fibers orientations at each stretch level. The direct comparison showed that the affine model did not predict correctly the evolution of the fibers orientation. Not surprisingly, it was at the largest stretches that we observed the greatest differences (see Figs. 7, 8, 9). At low stretch level (see Figs. 10, 11), the model and the observations were in general very close, although important differences were observed in case of important reorientations (higher than $10°$). Quantitative measurements on skin samples indicated that the differences between the predictions and the experimental observations appeared at the end of the heel region and increased in the linear region. These observations are consistent with the observation of two different responses of the tissue in the heel region and in the linear region (Bancelin et al. 2015; Lynch et al. 2016).

This limitation of the affine transformation assumption has been previously reported in studies on other types of tissues, in particular in the study of Chandran and Barocas (2005). The authors compared two models of a tissue equivalent, a gel of collagen fibers embedded in a matrix. On the one hand, they considered a model based on the affine assumption to predict the strain and reorientation in the tissue. On the other hand, they tested a network-based model that included information on the connection and force transmissions between fibers. The comparison of these two models led to significant differences in the model responses about the microstructural kinematic. Particularly, the fibers orientations, predicted by the two modeling approaches, presented some important differences. The fibers orientation in the network-based model seemed to be not correlated with the fibers strain. Therefore, these results indicated that the kinematic was not exclusively defined by the fibers strain. Thus, the authors highlighted the importance of identifying the relationship between the fibers network and the surrounding environment, to assess the role played by the fibers inter-connections on kinematic. In particular, for tissues which force transmission to fibers is mainly done by other fibers, the affine assumption appears greatly limited, and the impact of the organization in an interconnected network cannot be discarded. On the opposite, if the force transmission comes mainly from the global loading conditions, then fibers will more likely act independently and enforce the assumption of an affine kinematic.

The response of the fibers to the strain thus depends on the type of tissues. In certain types of tissue like pericardium, a good correlation was found between experimental measurements and simulation with the affine transformation model (Fan and Sacks 2014). In the study by Billiar and

Sacks (1997), the simulations of biaxial tensile tests coupled with a reorientation model under the affine assumption allowed to get fibers reorientation very close to experimental observations made by small angle light scattering (SALS). In the present work, we studied two other types of plane collagenous tissues. It is noteworthy that the affine assumption overestimates the reorientation for skin samples, while it underestimates it for liver capsules. It appears very likely that this difference of behaviors with respect to the affine assumption might come from tissue compositional differences. This can originate from many sources, including a possible difference in collagen fibers nature, the presence or not of elastin fibers, and the differences in collagen cross-links nature and content or even in other extracellular matrix components. The specific organizations of the fiber networks could also be a primary cause for this different reaction of the tissues relatively to the theoretical model, since the arrangement of fibers is significantly different between skin and liver capsule (Jayyosi et al. 2016; Lynch et al. 2016). The reorganization of the network seems to depend on other factors than only the applied strain to the individual fibers, at least for elementary volumes of few hundreds of micrometer. The degrees of freedom of the fibers are also defined by the network structure and the links between fibers, which can increase or prevent the reorientation of a given fiber in a particular direction.

Therefore, it would be interesting to investigate the relationship between strain and fiber orientation at a smaller scale. Our approach enables to probe scales which are significantly larger than the connectivity of the collagen network, and thus, we measure an average property. It could be interesting to probe a smaller scale, at which for example strain heterogeneity and discontinuous fibers sliding may play a significant role. Images with a higher resolution could also enable to make a better distinction between undulations (or crimps) of individual fibers and superposition of fibers with different orientations.

It is noteworthy that the tissue preparation and mechanical stimulation are significantly different between liver capsule and skin. It might induce differences in the material responses, in particular in the observed fiber motion with stretch. The different testing protocols, i.e., uniaxial testing on skin and biaxial inflation for liver capsule, might therefore be a secondary source of explanation to the tissues different response and to the under or over estimation of the fiber reorientation. Indeed, the biaxial loading might involve more structural effects than uniaxial loading.

Eventually, it appears from those results that the consideration of a reorientation model based solely on geometry seems quite limited to describe accurately the kinematic of fibers in planar fibrous tissues. Structural effects take indeed a huge part in the network reorganization, and the affine assumption presents important limitations when it does not take into account the interactions between fibers that influence the kinematic greatly. Affine assumption may be indeed relevant for small representative volumes, smaller than the fibers mesh size. However, at such small scale, the samples are unlikely to remain homogeneous in mechanical properties. At larger scales—as the ones we have been considering—the spatial organization of the fibers and the stress transmission by the extracellular matrix are likely to play significant roles on the fiber reorganization with stretch. Therefore, more complex assumptions including stresses transmission in the fibers mesh will provide more accurate results.

5 Conclusion

The affine transformation assumption that allows linking the fiber strain to the global transformation of the tissue seems to present important limitations. Using multiphoton microscopy imaging combined with mechanical assays, we measured independently the strain and the fibers orientations at different stretching. Results indicate that the fibers' kinematic is not entirely affine, but is over or underestimated depending on the tissue.

The structural phenomena induced by the interactions between fibers are then likely to be predominant in the deformation mechanisms of planar fibrous tissues. The affine assumption appears to be appropriate only in some specific cases, since it neglects the impact of the surrounding environment. Therefore, the development of constitutive models of planar fibrous tissues based on microstructure must include information about these interactions to predict faithfully the tissue behavior and link the macroscopic response to the microscopic organization.

Acknowledgements The authors wish to thank Pr Mathias Brieu for useful discussions. This work was supported by the Programme Avenir Lyon Saint-Etienne (ANR-11-IDEX-0007) of Université de Lyon, within the program "Investissements d'Avenir" operated by the French National Research Agency (ANR), and by grants from Ecole Polytechnique (interdisciplinary project) and from Agence Nationale de la Recherche (ANR-13-BS09-0004-02 and ANR-10-INBS-04).

Conflict of interest None of the authors have any professional or financial conflict of interest.

References

Alavi SH, Sinha A, Steward E et al (2015) Load-dependent extracellular matrix organization in atrioventricular heart valves: differences and similarities. Am J Physiol Heart Circ Physiol 309:H276–84. doi:10.1152/ajpheart.00164.2015

Bancelin S, Lynch B, Bonod-Bidaud C et al (2015) Ex vivo multiscale quantitation of skin biomechanics in wild-type and genetically-modified mice using multiphoton microscopy. Sci Rep 5:17635. doi:10.1038/srep17635

Benoit A, Latour G, Marie-Claire SK, Allain JM (2016) Simultaneous microstructural and mechanical characterization of human corneas

at increasing pressure. J Mech Behav Biomed Mater 60:93–105. doi:10.1016/j.jmbbm.2015.12.031

Billiar KL, Sacks MS (1997) A method to quantify the fiber kinematics of planar tissues under biaxial stretch. J Biomech 30:753–756. doi:10.1016/S0021-9290(97)00019-5

Butler DL, Goldstein Sa, Guilak F (2001) Functional tissue engineering: the role of biomechanics in articular cartilage repair. Clin Orthop Relat Res 122:S295–S305. doi:10.1115/1.1318906

Chandran PL, Barocas VH (2005) Affine versus non-affine fibril kinematics in collagen networks: theoretical studies of network behavior. J Biomech Eng 128:259. doi:10.1115/1.2165699

Chauvet D, Carpentier A, Allain J-M et al (2010) Histological and biomechanical study of dura mater applied to the technique of dura splitting decompression in Chiari type I malformation. Neurosurg Rev 33:287–294. doi:10.1007/s10143-010-0261-x (discussion 295)

Deyl Z, Macek K, Adam M, Vancíková O (1980) Studies on the chemical nature of elastin fluorescence. Biochim Biophys Acta 625:248–54

Fan R, Sacks MS (2014) Simulation of planar soft tissues using a structural constitutive model: finite element implementation and validation. J Biomech 47:2043–2054. doi:10.1016/j.jbiomech.2014.03.014

Fung YC (1990) Biomechanics: motion, flow, stress, and growth. Springer, New York

Gasser TC (2011) An irreversible constitutive model for fibrous soft biological tissue: a 3-D microfiber approach with demonstrative application to abdominal aortic aneurysms. Acta Biomater 7:2457–66. doi:10.1016/j.actbio.2011.02.015

Gasser TC, Ogden RW, Ga Holzapfel (2006) Hyperelastic modelling of arterial layers with distributed collagen fibre orientations. J R Soc Interface R Soc 3:15–35. doi:10.1098/rsif.2005.0073

Gelse K, Pöschl E, Aigner T (2003) Collagens—structure, function, and biosynthesis. Adv Drug Deliv Rev 55:1531–1546. doi:10.1016/j.addr.2003.08.002

Goulam Houssen Y, Gusachenko I, Schanne-Klein M-C, Allain J-M (2011) Monitoring micrometer-scale collagen organization in rat-tail tendon upon mechanical strain using second harmonic microscopy. J Biomech 44:2047–2052. doi:10.1016/j.jbiomech.2011.05.009

Hannafin JA, Arnoczky SP (1994) Effect of cyclic and static tensile loading on water content and solute diffusion in canine flexor tendons: an in vitro study. J Orthop Res 12:350–6. doi:10.1002/jor.1100120307

Holzapfel GA, Stadler M, Schulze-Bauer CAJ (2002) A layer-specific three-dimensional model for the simulation of balloon angioplasty using magnetic resonance imaging and mechanical testing. Ann Biomed Eng 30:753–767. doi:10.1114/1.1492812

Humphrey JD (2003) Review paper: continuum biomechanics of soft biological tissues. Proc R Soc A Math Phys Eng Sci 459:3–46. doi:10.1098/rspa.2002.1060

Jayyosi C (2015) Caractérisation mécanique et microstructurale du comportement à rupture de la capsule de Glisson pour la prédiction du risque de lésions des tissus hépatiques humains. Université Claude Bernard Lyon 1

Jayyosi C, Coret M, Bruyère-Garnier K (2016) Characterizing liver capsule microstructure via in situ bulge test coupled with multiphoton imaging. J Mech Behav Biomed Mater 54:229–243. doi:10.1016/j.jmbbm.2015.09.031

Jayyosi C, Fargier G, Coret M, Bruyère-Garnier K (2014) Photobleaching as a tool to measure the local strain field in fibrous membranes of connective tissues. Acta Biomater 10:2591–601. doi:10.1016/j.actbio.2014.02.031

Keyes JT, Lockwood DR, Simon BR, Vande Geest JP (2013) Deformationally dependent fluid transport properties of porcine coronary arteries based on location in the coronary vasculature. J Mech Behav Biomed Mater 17:296–306. doi:10.1016/j.jmbbm.2012.10.002

Lanir Y, Salant EL, Foux A (1988) Physico-chemical and microstructural changes in collagen fiber bundles following stretch in-vitro. Biorheology 25:591–603

Loerakker S, Ristori T, Baaijens FPT (2016) A computational analysis of cell-mediated compaction and collagen remodeling in tissue-engineered heart valves. J Mech Behav Biomed Mater 58:173–187. doi:10.1016/j.jmbbm.2015.10.001

Lynch B, Bancelin S, Bonod-Bidaud C et al (2016) A novel microstructural interpretation for the biomechanics of mouse skin derived from multiscale characterization. Acta Biomater. doi:10.1016/j.actbio.2016.12.051

Mauri a, Perrini M, Mateos JM (2013) Second harmonic generation microscopy of fetal membranes under deformation: normal and altered morphology. Placenta 34:1020–1026. doi:10.1016/j.placenta.2013.09.002

Mauri A, Ehret AE, Perrini M et al (2015) Deformation mechanisms of Human amnion: quantitative studies based on second harmonic generation microscopy. J Biomech. doi:10.1016/j.jbiomech.2015.01.045

Obbink-Huizer C, Oomens CWJ, Loerakker S et al (2014) Computational model predicts cell orientation in response to a range of mechanical stimuli. Biomech Model Mechanobiol 13:227–236. doi:10.1007/s10237-013-0501-4

Puxkandl R, Zizak I, Paris O et al (2002) Viscoelastic properties of collagen: synchrotron radiation investigations and structural model. Philos Trans R Soc Lond B Biol Sci 357:191–197. doi:10.1098/rstb.2001.1033

Ramanujan S (1914) Modular equations and approximations to pi. Q J Math 45:350–372

Raub CB, Unruh J, Suresh V et al (2008) Image correlation spectroscopy of multiphoton images correlates with collagen mechanical properties. Biophys J 94:2361–2373. doi:10.1529/biophysj.107.120006

Rezakhaniha R, Agianniotis a, Schrauwen JTC et al (2012) Experimental investigation of collagen waviness and orientation in the arterial adventitia using confocal laser scanning microscopy. Biomech Model Mechanobiol 11:461–473. doi:10.1007/s10237-011-0325-z

Robert L (2002) Elastin, past, present and future. Pathol Biol 50:503–511. doi:10.1016/S0369-8114(02)00336-X

Sacks MS (2003) Incorporation of experimentally-derived fiber orientation into a structural constitutive model for planar collagenous tissues. J Biomech Eng 125:280. doi:10.1115/1.1544508

Screen HRC, Evans SL (2009) Measuring strain distributions in tendon using confocal microscopy and finite elements. J Strain Anal Eng Des 44:327–335. doi:10.1243/03093247JSA491

Tang T, Ebacher V, Cripton P et al (2015) Shear deformation and fracture of human cortical bone. Bone 71:25–35. doi:10.1016/j.bone.2014.10.001

Vijayaraghavan S, Huq R, Hausman MR (2014) Methods of peripheral nerve tissue preparation for second harmonic generation imaging of collagen fibers. Methods 66:246–255. doi:10.1016/j.ymeth.2013.08.012

Voss B, Rauterberg J, Allam S, Pott G (1980) Distribution of collagen type I and type III and of two collagenous components of basement membranes in the human liver. Pathol Res Pract 170:50–60. doi:10.1016/S0344-0338(80)80155-5

Zoumi A, Lu X, Kassab GS, Tromberg BJ (2004) Imaging coronary artery microstructure using second-harmonic and two-photon fluorescence microscopy. Biophys J 87:2778–2786. doi:10.1529/biophysj.104.042887

Zoumi A, Yeh A, Tromberg BJ (2002) Imaging cells and extracellular matrix in vivo by using second-harmonic generation and two-photon excited fluorescence. Proc Natl Acad Sci USA 99:11014–11019. doi:10.1073/pnas.172368799